

# GAST: Sequential Gaussian Avatars with Hierarchical Spatio-temporal Context

Wangze Xu,<sup>1\*</sup> Yifan Zhan,<sup>1,2</sup> Zhihang Zhong,<sup>1†</sup> Xiao Sun<sup>1†</sup>  
<sup>1</sup>Shanghai Artificial Intelligence Laboratory <sup>2</sup>The University of Tokyo

## Abstract

*3D human avatars, through the use of canonical radiance fields and per-frame observed warping, enable high-fidelity rendering and animating. However, existing methods, which rely on either spatial SMPL(-X) poses or temporal embeddings, respectively suffer from coarse rendering quality or limited animation flexibility. To address these challenges, we propose GAST, a framework that unifies 3D human modeling with 3DGS by hierarchically integrating both spatial and temporal information. Specifically, we design a sequential conditioning framework for the non-rigid warping of the human body, under whose guidance more accurate 3D Gaussians can be obtained in the observation space. Moreover, the explicit properties of Gaussians allow us to embed richer sequential information, encompassing both the coarse sequence of human poses and finer per-vertex motion details. These sequence conditions are further sampled across different temporal scales, in a coarse-to-fine manner, ensuring unbiased inputs for non-rigid warping. Experimental results demonstrate that our method combined with hierarchical spatio-temporal modeling surpasses concurrent baselines, delivering both high-quality rendering and flexible animating capabilities.*

## 1. Introduction

Recent research on digital humans has highlighted the efficiency of 3D Gaussian Splatting [23] (3DGS), demonstrating its capability for high-quality and real-time rendering. By defining T-pose human Gaussians in a canonical space and employing specific warping techniques, we can render human avatars under various observations. The canonical Gaussian units and warping weights are jointly optimized under supervision from human video input.

The primary bottleneck in this task stems from the limited modeling of non-rigid warping, requiring a trade-off between rendering quality and animating capability. One stream of approaches [17, 44] introduces the prior from SMPL(-X) [37, 42] poses, leveraging human poses to guide

motions of each observation and relying on Linear Blend Skinning (LBS) for motion warping. Although they are well-suited for pose-driven animation, they often struggle with per-frame non-rigid warping in scenarios with complex garments. Other approaches [33, 51] utilize temporal embeddings instead of SMPL poses to model each frame independently, achieving high-quality rendering but making it challenging to animate avatars.

We experimentally find that the existing human pose condition [17, 44] and temporal embeddings are insufficient to fully capture the expression of human motion. On the one hand, while the human pose represents the spatial information of a template body, it fails to capture local details (e.g., garment deformation). On the other hand, existing temporal embeddings [33, 51] maintain temporal continuity in rendering by sacrificing geometric awareness of the human body, limiting their effectiveness for animation. In this paper, we aim to strike an ideal balance in both rendering and animating of human avatars by introducing a hierarchical spatio-temporal context. To this end, we refine the input conditions for non-rigid warping by modeling a motion sequence, ensuring correspondence of Gaussians across different observations.

The desired motion sequence should encapsulate rich spatio-temporal information to effectively guide the non-rigid warping process. Previous NeRF[38]-based methods [5] construct the motion sequence with human pose residuals to represent human motion. However, the human pose, as an inherently global representation, struggles to capture finer motion details. The explicit structure of 3DGS enables localized temporal modeling, facilitating the construction of a hierarchical motion sequence by encoding motion residuals from template vertices in SMPL(-X). This coarse-to-fine, pose-to-vertex design (as illustrated in Fig. 1) for the motion sequence captures hierarchical spatial motion while guaranteeing temporal continuity. How to determine the optimal stride for motion sequence remains a significant challenge. The motion sequence with a larger stride captures longer motion but loses details between adjacent frames, whereas the motion sequence with a smaller stride covers a shorter motion range but retains richer inter-frame details. To further incorporate detailed human motion, we

\*This work was done during the author’s internship at Shanghai Artificial Intelligence Laboratory. † denotes co-corresponding authors.

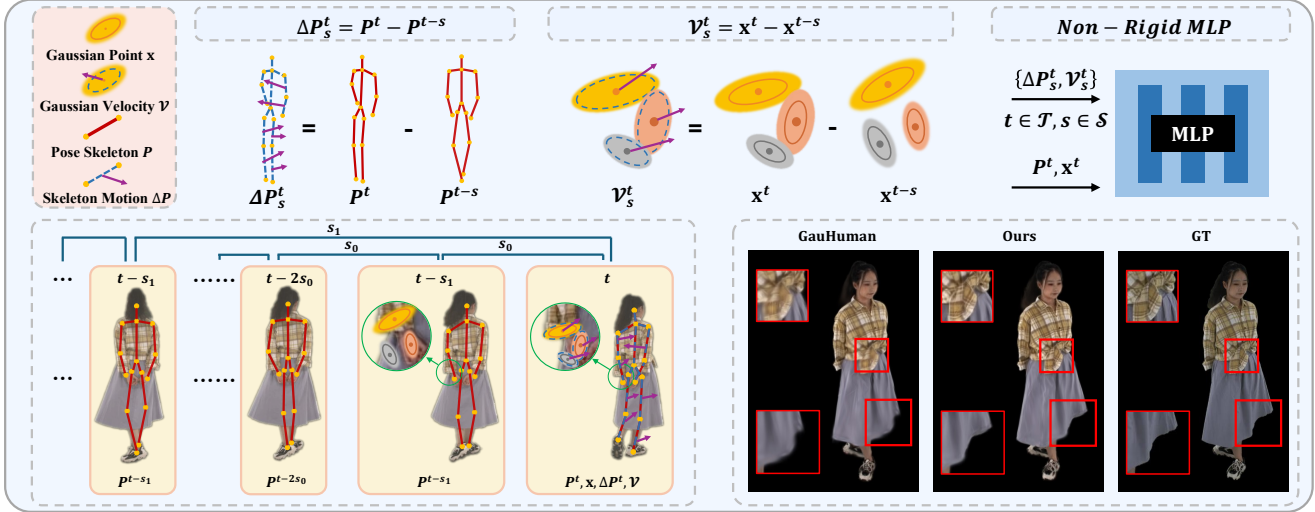


Figure 1. **Illustration of the Hierarchical Spatio-temporal Context Design.** We model the motion-dependent appearance variations with both coarse skeleton condition  $\Delta P$  and fine-grained point-wise velocity condition  $\mathcal{V}$ .  $\Delta P$  describes the overall human pose motion, which is derived from the difference between the human poses at adjacent frames.  $\mathcal{V}$  is the point-wise velocity that indicates finer-grained motion in local regions. Based on  $\Delta P$  and  $\mathcal{V}$ , we utilize an MLP to predict more accurate non-rigid deformation of each Gaussian primitive. To achieve robust deformation, we sample the overall motion trend and inter-frame details via diverse time intervals  $s$  for  $\Delta P$  and  $\mathcal{V}$ . The rendering results demonstrate that our method excels in regions with complex texture details as well as in areas where the appearance varies dramatically with motions.

propose a multi-scale sampling strategy for the motion sequence. The final input to the non-rigid network consists of motion sequences sampled at multiple temporal scales, arranged in a coarse-to-fine manner. This hierarchical temporal design combines both motion range and inter-frame details, further enhancing the model’s generalization ability in rendering from novel views.

We test our pipeline, GAST, on I3D-Human dataset [5] and DNA-Rendering dataset [6], which contain complex garments motions beyond the scope of the template body. Our method outperforms other baselines on these datasets, achieving compatibility in both rendering and animating. To summarize, our contributions are three-fold as follows:

- 1) GAST, the first framework for sequential Gaussian avatars, achieving a balance between high-fidelity rendering and animation through spatio-temporal context;
- 2) a hierarchical motion sequence that combines global human pose and localized vertex residuals, guiding non-rigid warping from coarse to fine;
- 3) a multi-scale sampling strategy for selecting strides for motion sequences, integrating both broader motion dynamics and finer inter-frame details.

## 2. Related Work

### 2.1. Human Avatars Based on SMPL(-X)

Recent advances in digital human modeling have benefited greatly from the SMPL(-X) series [37, 42], which

represents the human body by decomposing it into distinct shape components and pose-related motions, utilizing 3D mesh scanning techniques and principal component analysis (PCA). The *pose blend shapes* in SMPL(-X) enable human body deformation through a linear blend of poses of different joints, significantly improving the efficiency of animating digital humans. The widespread adoption of SMPL(-X) has further been boosted for human body animation, driven by methods [7, 46] that estimate parameters of SMPL(-X) from 2D image inputs. Despite its wide applications, the SMPL(-X) framework has its limitations. The skin-tight 3D meshes, based on pose blend shapes, struggle to model bodies with garments or accessories. This brings a challenge for complex human rendering based on SMPL(-X), particularly when dealing with garments and accessories.

### 2.2. SMPL(-X) Poses Guided Neural Human

Implicit neural methods, such as NeRF [38] and 3DGS [23], have become key contributors to digital human reconstruction due to their high-quality rendering capabilities. Some methods get inspiration from SMPL(-X) to build neural animatable 3D human avatars. These approaches typically map the T-pose to a canonical space and apply LBS weights to perform rigid transformations. Animation is then realized by mapping points from the canonical space to the observation space, with each frame’s human pose determining the transformation. NeRF-based ap-

proaches [2–5, 9, 12–14, 25, 43, 49] focus on reconstructing human avatars from monocular or multi-view synchronized videos. For more accurate human geometry, [47] incorporate smooth priors from neural Signed Distance Functions (SDF). More recent advances [16–18, 21, 22, 24, 27–29, 32, 34, 35, 39, 40, 44, 53–55] leverage 3DGS, resulting in faster and high-fidelity human rendering. We also notice that some works [5, 18] model a human pose sequence as the context to improve rendering quality. But they suffer from low-speed rendering and lack fine details of motion caused by simply integrating coarse human pose embedding with NeRF.

### 2.3. Human Rendering with Temporal Embeddings

The earliest modeling of dynamic radiance field [1, 8, 10, 11, 20, 30, 31, 36, 41, 45, 50] can be traced back to temporal embeddings in general scenes, where each frame’s observation is obtained by constructing a canonical space and a time-conditioned deformation field. Motivated by these, a stream of human researches [33, 51] focus on pure rendering quality, employing temporal embeddings instead of human pose to encode each frame of human videos. These methods often achieve high-quality, temporally continuous rendering. However, they struggle with the lack of geometric constraints from human pose, making parameterized animating unfeasible.

## 3. Preliminary

**SMPL(-X) Series** [37, 42] adopt a parameterized framework to represent human bodies across diverse shapes and poses. For each frame, the human mesh is derived by deforming a canonical template mesh based on shape and pose parameters. Specifically, a 3D point  $\mathbf{x}$  on the canonical mesh is warped to the corresponding point on the deformed mesh in the observation space, following

$$\text{LBS}(\mathbf{x}, \mathbf{B}_k, \omega_k(\mathbf{x})) = \sum_{k=1}^K \omega_k(\mathbf{x}) \mathbf{B}_k \mathbf{x}, \quad (1)$$

where  $K$  is the total bone number and  $\mathbf{B}_k$  is the transformation matrix for each bone. Specifically,  $\mathbf{B}_k$  consists of a rotation and translation matrix  $\mathbf{R}_k$  and  $\mathbf{b}_k$ . Here,  $\mathbf{R}_k$  represents the global rotation of each joint, influenced by the local joint rotations  $\mathbf{r}$ , while  $\mathbf{b}_k$  denotes each joint’s translation, determined by the joint positions  $\mathbf{j}$  and the human shape parameters  $\beta$ . Note that the linear blending weight  $\omega^k$  depends on  $\mathbf{x}$  and is regressed from comprehensive human meshes.

**3D Gaussian Splatting** [23] utilizes a set of point-based Gaussian primitives to explicitly represent scenes, enabling real-time and high-quality rendering. Each Gaussian primitive is defined by its center position  $\mathbf{x} \in \mathbb{R}^3$  and covariance matrix  $\Sigma \in \mathbb{R}^{3 \times 3}$ .

To ensure positive semi-definiteness and simplify optimization, the covariance matrix  $\Sigma$  is decomposed into a rotation matrix  $\mathbf{R}$  and a scaling matrix  $\mathbf{S}$  following

$$\Sigma = \mathbf{R} \mathbf{S} \mathbf{S}^T \mathbf{R}^T, \quad (2)$$

where  $\mathbf{R}$  and  $\mathbf{S}$  are derived by a scaling vector  $\mathbf{s} \in \mathbb{R}^3$  and a quaternion vector  $\mathbf{r} \in \mathbb{R}^4$  in practice. Additionally, each Gaussian primitive is also assigned a color feature  $sh \in \mathbb{R}^k$  represented by spherical harmonics (SH) and an opacity  $\alpha$  for rendering. During the rendering process, a splatting technique [23] is used to project each Gaussian primitive onto the 2D image space with a viewing transform  $\mathbf{W}$  and the Jacobian  $\mathbf{J}$  of the projective transformation’s affine approximation. The transformed covariance  $\Sigma'$  in the camera’s coordinates is

$$\Sigma' = \mathbf{J} \mathbf{W} \Sigma \mathbf{W}^T \mathbf{J}^T. \quad (3)$$

After projection, the pixel color  $C$  is computed by blending  $N$  ordered Gaussian primitives overlapping at the pixel as

$$C = \sum_{i \in N} c_i \alpha'_i \prod_{j=1}^{i-1} (1 - \alpha'_j), \quad (4)$$

where  $c_i$  is computed from SH feature  $sh$  and  $\alpha'_i$  is the product of  $\alpha_i$  and probability density of  $i$ -th 2D Gaussian.

For optimization, a photometric loss is defined by a combination of  $L_1$  and SSIM [48] losses:

$$L_{photo} = \lambda_1 L_1(\hat{I}, I) + (1 - \lambda_1)(1 - SSIM(\hat{I}, I)), \quad (5)$$

where  $\hat{I}$  and  $I$  denote the rendered and ground-truth images, and  $\lambda_1$  controls the balance between the two terms.

## 4. Method

Fig. 2 shows the framework of our method. We use the explicit point-based 3DGS as the representation of the human body. Given a collection of input cameras and images, we optimize a set of Gaussian primitives  $\{\mathcal{G}_i\}_{i=1}^{i=n}$  to fit the body’s shape and appearance. Each Gaussian primitive  $\mathcal{G}_i$  includes the center position  $\mathbf{x}$ , scaling vector  $\mathbf{s}$ , rotation quaternion vector  $\mathbf{r}$ , color feature  $sh$  and opacity  $\alpha$ , where  $\mathbf{x}$  is initialized from the SMPL template vertices  $\{\mathbf{T}_i\}_{i=1}^{i=N}$ . During the optimization process, we first apply non-rigid deformation with hierarchical spatio-temporal conditions to capture more accurate and fine-grained details (Sec. 4.1). Next, we adopt Linear Blend Skinning (LBS) to map canonical Gaussian primitives  $\mathcal{G}$  to observation space and render images via differentiable splitting (Sec.4.3).

### 4.1. Non-Rigid Deformation with Hierarchical Spatio-temporal Context

**Coarse Skeleton Motion.** As illustrated in Fig. 1, we introduce a coarse-to-fine spatio-temporal context to excavate

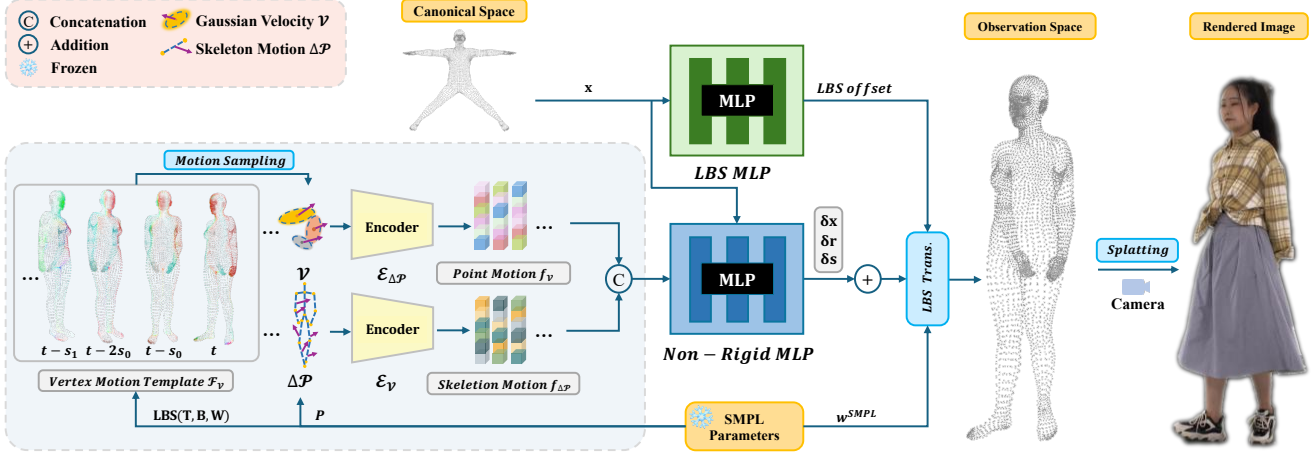


Figure 2. **Overview of GAST.** We first initialize canonical Gaussian positions  $\mathbf{x}$  with SMPL template vertices. We propose a hierarchical spatio-temporal context for non-rigid deformation to better capture complex human motion. The skeleton motion condition  $f_{\Delta\mathcal{P}}$  aims to distinguish the appearance variation caused by overall body movement. The point motion condition  $f_V$ , sampled from the vertex motion template  $\mathcal{F}_V$  (points in different colors represent different motions), is designed to capture finer-grained temporal information in local regions. We utilize an MLP  $\mathcal{E}_{non-rigid}$  to predict the non-rigid deformation of each Gaussian based on both  $f_{\Delta\mathcal{P}}$  and  $f_V$  conditions. The non-rigid deformed Gaussians are then warped into observation space via the standard LBS transformation for rendering.

additional conditions for non-rigid deformation. Typically, most human 3D avatar methods use the current frame pose as a condition to predict non-rigid deformation [17, 44]. While this provides spatial information to distinguish the motion of different body parts, it fails to capture temporal motion changes, as discussed in [5]. Therefore, given a frame at time  $t$ , we consider a sequence of regularly interval-sampled frames  $\mathcal{T}$  to model inter-frame body motion variations, defined as

$$\mathcal{T} = \{t - s, t - 2s, \dots, t - Ls\}, \quad (6)$$

where  $L$  is the sequence length and  $s$  is the time interval. The coarse motion of body skeletons at each time step  $t \in \mathcal{T}$  can be derived by calculating the difference of poses between adjacent frames (as illustrated in Fig. 1), following

$$\Delta\mathcal{P} = \{\Delta P^t = \delta(P^t, P^{t-s}) | t \in \mathcal{T}\}, \quad (7)$$

where  $P \in \mathbb{R}^{K \times 3}$  is the body pose and  $\delta$  denotes the difference  $\Delta\mathcal{P}$  between two poses in axis-angle form. We employ an MLP  $\mathcal{E}_{\Delta\mathcal{P}}$  to encode the sequential skeleton motion  $\Delta\mathcal{P} \in \mathbb{R}^{L \times K \times 3}$ , flattened along the temporal dimension, into a skeleton motion embedding  $f_{\Delta\mathcal{P}} \in \mathbb{R}^{32}$ , which serves as a condition for the subsequent non-rigid deformation. Further details are provided in the supplementary material.

**Fine Vertex Motion.** Compared to previous implicit NeRF-based methods, the point-based 3DGS representation enables us to explore more fine-grained temporal motion information. We derive a point-wise velocity vector  $v_i$  for each Gaussian primitive  $\mathcal{G}_i$  to model the fine-grained localized body motion, which is beyond the scope of pose

skeleton motion  $\Delta\mathcal{P}$ . By measuring the position variations across adjacent time steps, we calculate per-frame velocity

$$v^t = \frac{\mathbf{x}_o^t - \mathbf{x}_o^{t-s}}{s}, \quad (8)$$

where  $\mathbf{x}_o$  denotes the warped coordinates in observation space. However, since the positions of Gaussian primitives are updated during optimization, it is not stable to obtain  $v_i$  based on such a dynamic variable. Moreover, transforming the canonical Gaussians into the observation space requires non-rigid deformation first, which leads to a circular dependency and conflicts with the current velocity design. To this end, we introduce a motion template field  $\mathcal{F}_V = \{\mathbf{V}_i\}_{i=1}^N$  that stores the velocity of each SMPL vertex, and  $v_i$  for each Gaussian primitive is sampled from  $\mathcal{F}_V$  based on the distance between query points and vertices in this template. Specifically, given a time step  $t$  and the corresponding body pose  $P^t = \{(\mathbf{R}_k^t, \mathbf{b}_k^t) | k \in K\}$ , the SMPL template vertices in  $\mathbf{T}$  can be warped into observation space with the template skinning weights  $\mathbf{W}$  and standard linear blend skinning, following

$$\mathbf{T}_o^t = \text{LBS}(\mathbf{T}, \mathbf{B}^t, \mathbf{W}), \quad (9)$$

where  $\mathbf{B}^t$  is the transformation matrix derived from rotation and translation matrix  $\mathbf{R}^t$  and  $\mathbf{b}^t$ .  $\mathbf{W}$  is the template SMPL LBS weights. The velocity  $\mathbf{V}$  of each template vertices  $\mathbf{T}$  can be further derived as

$$\mathbf{V}^t = \frac{\mathbf{T}_o^t - \mathbf{T}_o^{t-s}}{s}. \quad (10)$$



We sample the velocity from this motion template field  $\mathcal{F}_{\mathbf{V}}$  for each Gaussian primitive. To obtain robust sampled velocities and model body’s local region information, we input the  $\tau$  nearest template vertexes’ velocities into an MLP  $\mathcal{E}_{knn}$  to learn a local velocity embedding

$$e_i^t = \mathcal{E}_{knn}(\{\mathbf{V}_j^t\}), \quad j \in \mathbf{KNN}(\mathbf{T}, \mathbf{x}_i), \quad (11)$$

where  $\mathbf{KNN}(\mathbf{T}, \mathbf{x}_i)$  denotes the  $\tau$  nearest SMPL template vertexes of the canonical Gaussian position  $\mathbf{x}_i$ . Then we apply an MLP  $\mathcal{E}_{\mathcal{V}}$  to encode each Gaussian primitive’s sequential motion state  $\mathcal{V} = \{e^t | t \in \mathcal{T}\}$  into a point-wise sequential condition  $f_{\mathcal{V}} \in \mathbb{R}^{64}$  for non-rigid deformation.

**Non-Rigid Deformation.** Given the coarse skeleton motion  $f_{\Delta\mathcal{P}} = \mathcal{E}_{\Delta\mathcal{P}}(\Delta\mathcal{P})$  condition and fine point-wise velocity condition  $f_{\mathcal{V}} = \mathcal{E}_{\mathcal{V}}(\mathcal{V})$ , we utilize an MLP to predict each Gaussian’s non-rigid deformation as

$$\delta\mathbf{x}, \delta\mathbf{s}, \delta\mathbf{r} = \mathcal{E}_{non-rigid}(\mathbf{x}, P, f_{\Delta\mathcal{P}}, f_{\mathcal{V}}). \quad (12)$$

The deformed canonical Gaussian  $\mathcal{G}'$  is

$$\mathbf{x}' = \mathbf{x} + \delta\mathbf{x}, \quad (13)$$

$$\mathbf{s}' = \mathbf{s} + \delta\mathbf{s}, \quad (14)$$

$$\mathbf{r}' = \mathbf{r} \cdot \delta\mathbf{r}, \quad (15)$$

where  $\cdot$  denotes the multiplication of two quaternions.

## 4.2. Multi-scale Sequence Sampling

To capture both the overall motion trend and the inter-frame motion details, we adopt a multi-scale sequence sampling strategy. Specifically, we sample a series of motion sequences at several progressively increasing intervals to get

$$\mathcal{S} = \{s = s_0 + i\Delta s\}_{i=0}^{i=m}, \quad (16)$$

where  $\Delta s$  is the increasing rate of sampling interval  $s$ . We then input the multi-scale sampled sequence motions into the encoder  $\mathcal{E}_{\Delta\mathcal{P}}$  and  $\mathcal{E}_{\mathcal{V}}$  to obtain hierarchical temporal motion embeddings

$$f_{\Delta\mathcal{P}} = \mathcal{E}_{\Delta\mathcal{P}}(\{\Delta\mathcal{P}_s\}), \quad (17)$$

$$f_{\mathcal{V}} = \mathcal{E}_{\mathcal{V}}(\{\mathcal{V}_s\}), \quad (18)$$

where  $s \in \mathcal{S}$ . In practice, we concatenate all skeleton motion conditions,  $\Delta\mathcal{P}_s$  for  $s \in \mathcal{S}$ , and localized vertex motion conditions,  $\mathcal{V}_s$  for  $s \in \mathcal{S}$ , across different sampling scales. These are then input to  $\mathcal{E}_{\Delta\mathcal{P}}$  and  $\mathcal{E}_{\mathcal{V}}$ , respectively. More details are shown in the supplementary material.

## 4.3. Optimization

**Rigid Deformation.** We utilize the standard LBS operation to map the non-rigid deformed Gaussians  $\mathcal{G}_o$  into the

observation space, following

$$\mathbf{x}_o = \mathbf{LBS}(\mathbf{x}', \mathbf{B}, \omega), \quad (19)$$

$$\mathbf{R}_o = \sum_{k=1}^K \omega_k(\mathbf{x}') \mathbf{B}_k \mathbf{R}', \quad (20)$$

where  $\mathbf{R}'$  is the rotation matrix derived from non-rigid deformed Gaussian’s rotation quaternion  $\mathbf{r}'$  and  $\mathbf{R}_o$  represents the rotation matrix in observation space. Following the previous method [17], we utilize an MLP  $\mathcal{E}_{lbs}$  to predict the LBS weight offsets for each query canonical point and update the sampled weights from the nearest SMPL vertex as

$$\omega_k(\mathbf{x}) = \omega_k^{SMPL}(\mathbf{x}) + \mathcal{E}_{lbs}(\mathbf{x}). \quad (21)$$

Similar to [5, 17, 49], we introduce a pose refinement MLP  $\mathcal{E}_{pose}$  to refine the pose estimate from SMPL for a better fit to the human body.

**Loss Function.** With the transformed Gaussian primitives  $\mathcal{G}_o$  in observation space, we apply the standard splitting [23] to render images as

$$I = \mathbf{Splatting}(\mathbf{x}_o, \mathbf{R}_o, s', \alpha, sh). \quad (22)$$

During the optimization process, we employ four loss functions as supervision, summarized as

$$\mathcal{L} = \lambda_1 \mathcal{L}_{color} + \lambda_2 \mathcal{L}_{ssim} + \lambda_3 \mathcal{L}_{lips} + \mathcal{L}_{mask}, \quad (23)$$

where  $\lambda$  is used to balance the weight of different losses.  $\mathcal{L}_{mask}$  [17] is an  $L_2$  loss between the rendered  $\alpha$  and human body mask. Additional details of the pipeline are provided in the supplementary material.

## 5. Experiments

### 5.1. Datasets

**DNA-Rendering** [6] is a challenging realistic human-centric rendering dataset. It contains diverse scenes from everyday life to professional occasions. We choose 6 typical sequences with loose-fitting garments (1.0206\_04, 2.0007\_04, 2.0019\_10, 2.0044\_11, 2.0051\_09, 2.0813\_05) for experiments. We adopt 24 views for training and 6 views for testing. Novel view rendering results compared with other baselines are reported.

**I3D-Human** [5] comprises multi-view video frames of humans with loose clothing and complex movements. Compared to previous datasets such as ZJU-MoCap [43], which are mainly collected under controlled speeds and tight-fitting garments, I3D-Human contains scenes closer to daily life. We conduct experiments on 4 sequences following the data split in Dyco [5] and all training and testing data are retained to be the same across all comparison methods. For each sequence, we use 4-5 views for training and the rest for testing.

Table 1. **Quantitative Results on DNA-Rendering Dataset.** We report the performance of novel view rendering. Our GAST outperforms previous state-of-the-art human modeling methods. We mark the **best** and the **second best** methods in cells. LPIPS\*=LPIPS  $\times 10^3$ .

Subject:	1_0206_04			2_0007_04			2_0019_10			2_0044_11			2_0051_09			2_0813_05		
Metric:	PSNR $\uparrow$	SSIM $\uparrow$	LPIPS* $\downarrow$	PSNR $\uparrow$	SSIM $\uparrow$	LPIPS* $\downarrow$	PSNR $\uparrow$	SSIM $\uparrow$	LPIPS* $\downarrow$	PSNR $\uparrow$	SSIM $\uparrow$	LPIPS* $\downarrow$	PSNR $\uparrow$	SSIM $\uparrow$	LPIPS* $\downarrow$	PSNR $\uparrow$	SSIM $\uparrow$	LPIPS* $\downarrow$
3DGS-Avatar [44]	26.68	0.9434	48.31	28.10	0.9487	53.86	32.09	0.9705	28.87	28.28	0.9506	35.68	25.06	0.9530	41.39	31.75	0.9692	29.94
GART [27]	27.19	0.9454	56.47	28.22	0.9525	56.46	31.13	0.9686	35.16	28.90	0.9561	41.27	26.47	0.9628	42.21	32.06	0.9729	35.74
GauHuman [17]	28.49	0.9534	46.45	28.32	0.9501	52.16	32.55	0.9716	27.91	31.02	0.9670	28.85	26.24	0.9610	38.21	33.79	0.9776	25.14
GAST(Ours)	30.81	0.9649	39.47	29.63	0.9566	43.72	34.97	0.9777	23.53	32.62	0.9747	23.83	28.45	0.9685	34.06	35.81	0.9843	20.83

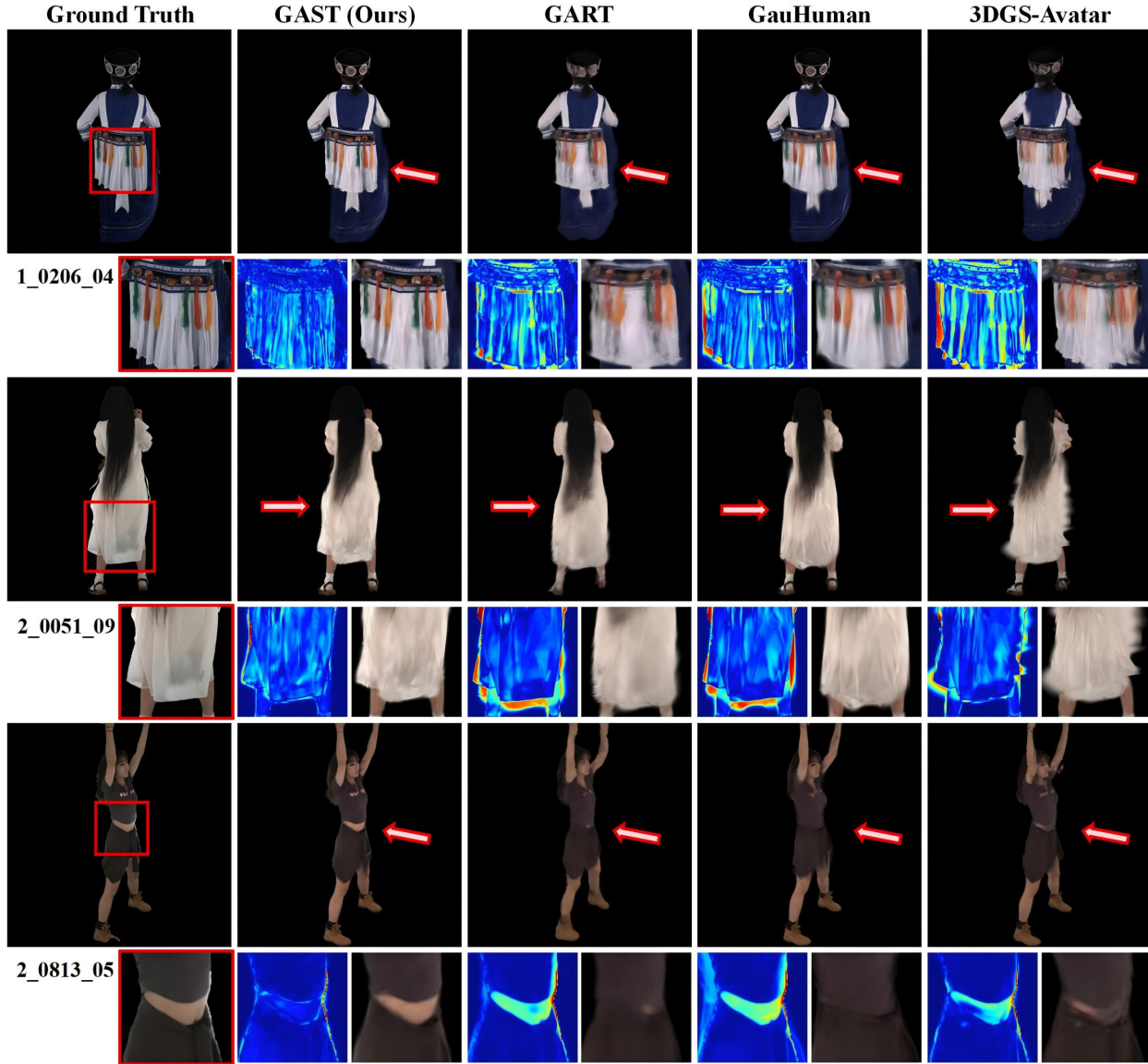


Figure 3. **Qualitative Results on DNA-Rendering Dataset [6].** We compare the visual quality of novel view rendering with previous SOTA methods. To present the differences more clearly, we zoom into the local region and compute the error maps compared with ground truth images. The results show that our method achieves competitive results on both the overall and local region qualities.

## 5.2. Baselines and Metrics

We compare against the state-of-the-art human modeling methods including Dyco [5], 3DGS-Avatar [44],

GART [27], and GauHuman [17]. Dyco is an implicit NeRF-based method that adopts pose sequence information for temporal modeling. We compare performance with Dyco to showcase the better efficacy of our point-based

Table 2. **Quantitative Results on I3D-Human Dataset.** We report the performance of novel view rendering. The proposed method achieves competitive results compared with Dyco [5], GauHuman [17], and 3DGS-Avatar [44].

Subject: Metric:	ID1_1			ID1_2			ID2_1			ID3_1		
	PSNR $\uparrow$	SSIM $\uparrow$	LPIPS* $\downarrow$	PSNR $\uparrow$	SSIM $\uparrow$	LPIPS* $\downarrow$	PSNR $\uparrow$	SSIM $\uparrow$	LPIPS* $\downarrow$	PSNR $\uparrow$	SSIM $\uparrow$	LPIPS* $\downarrow$
3DGS-Avatar [44]	29.78	0.9600	31.40	31.29	0.9627	28.09	29.63	0.9604	37.33	32.73	0.9602	39.47
Dyco [5]	31.53	0.9648	25.17	31.76	0.9646	25.60	29.95	0.9651	29.46	32.78	0.9631	33.06
GauHuman [17]	29.47	0.9571	39.46	30.42	0.9585	38.87	28.51	0.9546	49.46	32.10	0.9546	53.67
GAST(Ours)	31.81	0.9652	28.64	31.88	0.9636	30.01	31.35	0.9669	34.04	33.47	0.9633	37.90

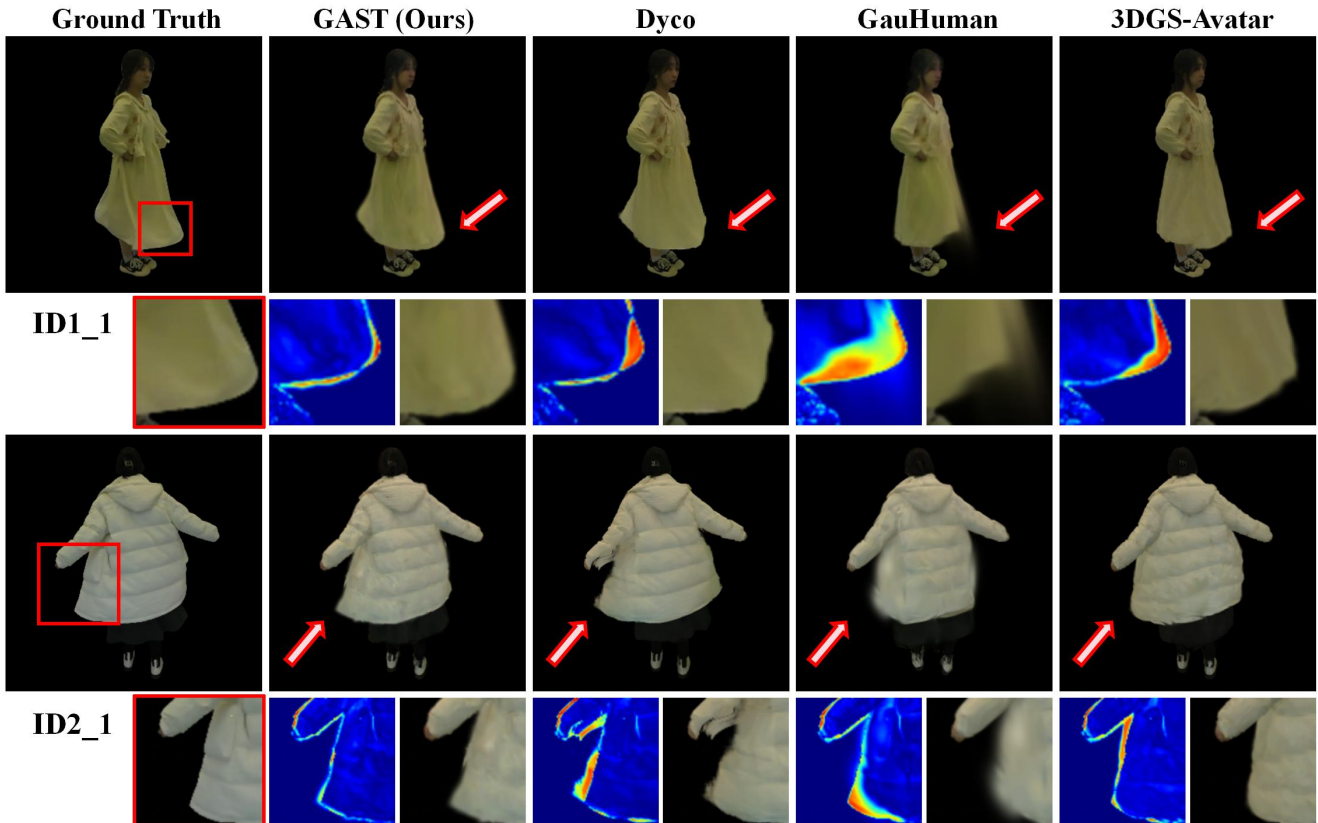


Figure 4. **Qualitative Results on I3D-Human Dataset [5].** We compare the visual quality of novel view rendering with SOTA methods.

fine-grained spatio-temporal context design. 3DGS-Avatar, GART, and GauHuman are explicit 3DGS-based methods, and all of them are originally designed for monocular inputs. For fairness, we extend them to multi-view input under the same settings. We compare these methods to demonstrate that finer rendering details can be achieved with our hierarchical sequential conditions for Gaussian points.

We report three key metrics: peak signal-to-noise ratio (PSNR), structural similarity index measure (SSIM) [48], and learned perceptual image patch similarity (LPIPS) [52].

### 5.3. Comparison

**Comparison on DNA-Rendering.** Tab. 1 shows the quantitative results on DNA-Rendering dataset. The pro-

posed GAST outperforms previous state-of-the-art human modeling methods across all metrics. To demonstrate the visual improvement, we compare the quality of rendering images in Fig. 3. Previous methods, which lack the temporal motion information for non-rigid deformations, are unable to predict the movement of Gaussian primitives properly, resulting in blurred renderings in regions with complex textures (scene 1\_0206\_04 in Fig. 3). Besides, the results in Fig. 3 show that the compared methods fail to capture the proper shape variation caused by movement (see the white dress in scene 2\_0051\_09). Although these methods achieve a smooth appearance in these areas, the error maps show that they fail to closely match the actual shape. We leverage the spatio-temporal context to predict Gaussian defor-

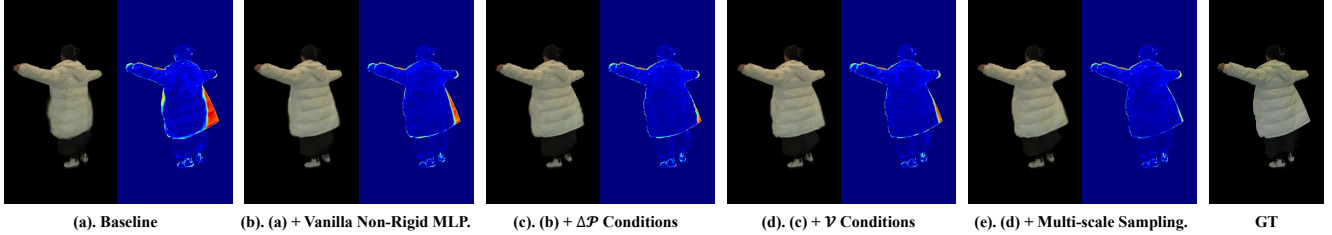


Figure 5. **Qualitative Ablation Results.** We compare the visual influence of different components on ID2\_1 scene of I3D-Human dataset.

mations, allowing our method to capture more accurate detailed appearance variations caused by human motions.

**Comparison on I3D-Human.** The quantitative results in Tab. 2 show that our method surpasses the previous SOTA method on most metrics, demonstrating our competitive performance on the I3D-Human dataset. Previous NeRF-based Dyco [5] utilizes pose variation as a condition to model human motions. However, it is limited to capturing only overall body motion trends and lacks the capacity for finer-grained modeling in local regions. For example, in ID1\_1 and ID2\_1 shown in Fig. 4, Dyco fails to model the information in regions far from the human body skeleton, leading to rendering results that do not accurately reflect the true motion. Our method designs more fine-grained conditions for the explicit point-based Gaussian representation to excavate both spatial and temporal motion information hierarchically. The rendering details in Fig. 4 demonstrate the improvement benefiting from such design in these local regions. More results are shown in supplementary materials.

Table 3. **Quantitative Ablation Results on I3D-Human Dataset.** The Vanilla Non-Rigid MLP in (b) only utilizes Gaussian positions  $\mathbf{x}$  and the current frame pose  $P$  as the conditions.

Methods	PSNR $\uparrow$	SSIM $\uparrow$	LPIPS* $\downarrow$
(a) Baseline	29.88	0.9570	38.12
(b) (a)+Vanilla Non-Rigid MLP.	31.18	0.9614	35.78
(c) (b)+ $\Delta\mathcal{P}$ Conditions.	31.89	0.9640	33.86
(d) (c)+ $\mathcal{V}$ Conditions.	32.05	0.9646	32.82
(e) (d)+Multi-scale Sampling. (Ours)	<b>32.13</b>	<b>0.9647</b>	<b>32.65</b>

## 5.4. Ablation Study

In this section, we ablate the influence of various components in our methods on I3D-Human dataset. Tab. 3 shows the average metrics of 4 sequences under different settings.

**Skeleton motion condition  $\Delta\mathcal{P}$**  denotes the overall human body movement. Compared to predicting non-rigid deformation only with the Gaussian position, incorporating this additional global temporal information allows our method to better model the overall human shape and achieve higher rendering quality, as demonstrated in Tab. 3 (c).

**Fine-grained point-wise motion condition  $\mathcal{V}$**  describes the local region’s variation in a more detailed manner. Such

point-based motion information captures the relationship between motion and appearance variations in areas beyond the human skeleton. Tab. 3 (d) and Fig. 5 (d) show that our method achieves higher rendering details in local regions.

**Multi-scale sequence sampling** is designed to capture both the overall motion trend and the fine-grained inter-frame motion details. With temporal conditions sampled at different intervals, our method is able to predict each Gaussian’s deformation more robustly, leading to better rendering quality as shown in Tab. 3 (e) and Fig. 5 (e).

## 6. Limitations and Conclusion

**Limitations.** Compared to prior NeRF-based approaches, our method models the human body with the point-based Gaussian representation, which may introduce needle-like artifacts during rendering. As indicated in Tab. 2, the metric on LPIPS is slightly inferior to that of NeRF-based Dyco [5]. We notice that some subsequent works [15, 19] on 3DGS optimize the artifacts by introducing surface-related smooth regularization. Generative model-based human avatar [26] could also potentially be introduced as a guarantee of high-fidelity rendering. However, these are beyond the scope of our motion modeling and will serve as future work to improve rendering quality.

**Conclusion.** In this paper, we propose GAST, a 3DGS-based framework that integrates hierarchical spatial-temporal information for 3D human modeling. Specifically, we introduce a coarse-to-fine motion context for the non-rigid deformation of Gaussian primitives. At the spatial dimension, the global and local region transformations for Gaussians are learned based on the overall inter-frame human pose variations and point-wise motions. To capture stable temporal motion information for each point, we introduce an SMPL vertex velocity template and sample the velocity of each Gaussian point from it. Along the temporal dimension, we apply a multi-scale sampling strategy to capture both long-term motion trends and inter-frame details, supporting more robust predictions of Gaussian deformations. Through the above design, we have achieved state-of-the-art rendering of human avatars with complex garments and motions.



## References

- [1] Ang Cao and Justin Johnson. Hexplane: A Fast Representation for Dynamic Scenes. In *Proceedings of the IEEE/CVF Conference on Computer Vision and Pattern Recognition*, pages 130–141, 2023. 3
- [2] Jianchuan Chen, Ying Zhang, Di Kang, Xuefei Zhe, Linchao Bao, Xu Jia, and Huchuan Lu. Animatable neural radiance fields from monocular rgb videos. *arXiv preprint arXiv:2106.13629*, 2021. 3
- [3] Xu Chen, Yufeng Zheng, Michael J Black, Otmar Hilliges, and Andreas Geiger. Snarf: Differentiable forward skinning for animating non-rigid neural implicit shapes. In *Proceedings of the IEEE/CVF International Conference on Computer Vision*, pages 11594–11604, 2021.
- [4] Xu Chen, Tianjian Jiang, Jie Song, Max Rietmann, Andreas Geiger, Michael J Black, and Otmar Hilliges. Fast-snarf: A fast deformer for articulated neural fields. *IEEE Transactions on Pattern Analysis and Machine Intelligence*, 45(10): 11796–11809, 2023.
- [5] Yutong Chen, Yifan Zhan, Zhihang Zhong, Wei Wang, Xiao Sun, Yu Qiao, and Yinqiang Zheng. Within the dynamic context: Inertia-aware 3d human modeling with pose sequence. *arXiv preprint arXiv:2403.19160*, 2024. 1, 2, 3, 4, 5, 6, 7, 8
- [6] Wei Cheng, Ruixiang Chen, Siming Fan, Wanqi Yin, Keyu Chen, Zhongang Cai, Jingbo Wang, Yang Gao, Zhengming Yu, Zhengyu Lin, et al. Dna-rendering: A diverse neural actor repository for high-fidelity human-centric rendering. In *Proceedings of the IEEE/CVF International Conference on Computer Vision*, pages 19982–19993, 2023. 2, 5, 6, 1
- [7] Junting Dong, Qi Fang, Wen Jiang, Yurou Yang, Hujun Bao, and Xiaowei Zhou. Fast and robust multi-person 3d pose estimation and tracking from multiple views. In *T-PAMI*, 2021. 2
- [8] Sara Fridovich-Keil, Giacomo Meanti, Frederik Rahbæk Warburg, Benjamin Recht, and Angjoo Kanazawa. K-planes: Explicit Radiance Fields in Space, Time, and Appearance. In *Proceedings of the IEEE/CVF Conference on Computer Vision and Pattern Recognition*, pages 12479–12488, 2023. 3
- [9] Guy Gafni, Justus Thies, Michael Zollhofer, and Matthias Nießner. Dynamic neural radiance fields for monocular 4d facial avatar reconstruction. In *Proceedings of the IEEE/CVF Conference on Computer Vision and Pattern Recognition*, pages 8649–8658, 2021. 3
- [10] Wanshui Gan, Hongbin Xu, Yi Huang, Shifeng Chen, and Naoto Yokoya. V4D: Voxel for 4D Novel View Synthesis. *IEEE Transactions on Visualization and Computer Graphics*, 2023. 3
- [11] Chen Gao, Ayush Saraf, Johannes Kopf, and Jia-Bin Huang. Dynamic View Synthesis from Dynamic Monocular Video. In *Proceedings of the IEEE/CVF International Conference on Computer Vision*, pages 5712–5721, 2021. 3
- [12] Qingzhe Gao, Yiming Wang, Libin Liu, Lingjie Liu, Christian Theobalt, and Baoquan Chen. Neural novel actor: Learning a generalized animatable neural representation for human actors. *IEEE Transactions on Visualization and Computer Graphics*, 2023. 3
- [13] Chen Geng, Sida Peng, Zhen Xu, Hujun Bao, and Xiaowei Zhou. Learning neural volumetric representations of dynamic humans in minutes. In *Proceedings of the IEEE/CVF Conference on Computer Vision and Pattern Recognition*, pages 8759–8770, 2023.
- [14] Shubham Goel, Georgios Pavlakos, Jathushan Rajasegaran, Angjoo Kanazawa, and Jitendra Malik. Humans in 4d: Reconstructing and tracking humans with transformers. In *Proceedings of the IEEE/CVF International Conference on Computer Vision*, pages 14783–14794, 2023. 3
- [15] Antoine Guédon and Vincent Lepetit. Gaussian frosting: Editable complex radiance fields with real-time rendering. *ECCV*, 2024. 8
- [16] Liangxiao Hu, Hongwen Zhang, Yuxiang Zhang, Boyao Zhou, Boning Liu, Shengping Zhang, and Liqiang Nie. Gaussianavatar: Towards realistic human avatar modeling from a single video via animatable 3d gaussians. In *Proceedings of the IEEE/CVF Conference on Computer Vision and Pattern Recognition*, pages 634–644, 2024. 3
- [17] Shoukang Hu, Tao Hu, and Ziwei Liu. Gauhuman: Articulated gaussian splatting from monocular human videos. In *Proceedings of the IEEE/CVF Conference on Computer Vision and Pattern Recognition*, pages 20418–20431, 2024. 1, 4, 5, 6, 7, 2
- [18] Tao Hu, Fangzhou Hong, and Ziwei Liu. Surmo: Surface-based 4d motion modeling for dynamic human rendering. In *Proceedings of the IEEE/CVF Conference on Computer Vision and Pattern Recognition*, pages 6550–6560, 2024. 3
- [19] Binbin Huang, Zehao Yu, Anpei Chen, Andreas Geiger, and Shenghua Gao. 2d gaussian splatting for geometrically accurate radiance fields. In *ACM SIGGRAPH 2024 Conference Papers*, pages 1–11, 2024. 8
- [20] Hankyu Jang and Daeyoung Kim. D-tensorf: Tensorial Radiance Fields for Dynamic Scenes. *arXiv preprint arXiv:2212.02375*, 2022. 3
- [21] Rohit Jena, Ganesh Subramanian Iyer, Siddharth Choudhary, Brandon Smith, Pratik Chaudhari, and James Gee. Splatarmor: Articulated gaussian splatting for animatable humans from monocular rgb videos. *arXiv preprint arXiv:2311.10812*, 2023. 3
- [22] HyunJun Jung, Nikolas Brasch, Jifei Song, Eduardo Perez-Pellitero, Yiren Zhou, Zhihao Li, Nassir Navab, and Benjamin Busam. Deformable 3d gaussian splatting for animatable human avatars. *arXiv preprint arXiv:2312.15059*, 2023. 3
- [23] Bernhard Kerbl, Georgios Kopanas, Thomas Leimkühler, and George Drettakis. 3d gaussian splatting for real-time radiance field rendering. *ACM Transactions on Graphics*, 42(4), 2023. 1, 2, 3, 5
- [24] Muhammed Kocabas, Jen-Hao Rick Chang, James Gabriel, Oncel Tuzel, and Anurag Ranjan. Hugs: Human gaussian splats. In *Proceedings of the IEEE/CVF conference on computer vision and pattern recognition*, pages 505–515, 2024. 3
- [25] Youngjoong Kwon, Dahun Kim, Duygu Ceylan, and Henry Fuchs. Neural human performer: Learning generalizable radiance fields for human performance rendering. *Advances*

- in *Neural Information Processing Systems*, 34:24741–24752, 2021. 3
- [26] Youngjoong Kwon, Baole Fang, Yixing Lu, Haoye Dong, Cheng Zhang, Francisco Vicente Carrasco, Albert Mosella-Montoro, Jianjin Xu, Shingo Takagi, Daeil Kim, et al. Generalizable human gaussians for sparse view synthesis. In *European Conference on Computer Vision*, pages 451–468. Springer, 2025. 8
- [27] Jiahui Lei, Yufu Wang, Georgios Pavlakos, Lingjie Liu, and Kostas Daniilidis. Gart: Gaussian articulated template models. In *Proceedings of the IEEE/CVF Conference on Computer Vision and Pattern Recognition*, pages 19876–19887, 2024. 3, 6
- [28] Mingwei Li, Jiachen Tao, Zongxin Yang, and Yi Yang. Human101: Training 100+ fps human gaussians in 100s from 1 view. *arXiv preprint arXiv:2312.15258*, 2023.
- [29] Mengtian Li, Shengxiang Yao, Zhifeng Xie, Keyu Chen, and Yu-Gang Jiang. Gaussianbody: Clothed human reconstruction via 3d gaussian splatting. *arXiv preprint arXiv:2401.09720*, 2024. 3
- [30] Tianye Li, Mira Slavcheva, Michael Zollhoefer, Simon Green, Christoph Lassner, Changil Kim, Tanner Schmidt, Steven Lovegrove, Michael Goesele, Richard Newcombe, et al. Neural 3D Video Synthesis from Multi-view Video. In *Proceedings of the IEEE/CVF Conference on Computer Vision and Pattern Recognition*, pages 5521–5531, 2022. 3
- [31] Zhengqi Li, Simon Niklaus, Noah Snavely, and Oliver Wang. Neural Scene Flow Fields for Space-time View Synthesis of Dynamic Scenes. In *Proceedings of the IEEE/CVF Conference on Computer Vision and Pattern Recognition*, pages 6498–6508, 2021. 3
- [32] Zhe Li, Zerong Zheng, Lizhen Wang, and Yebin Liu. Animatable gaussians: Learning pose-dependent gaussian maps for high-fidelity human avatar modeling. In *Proceedings of the IEEE/CVF Conference on Computer Vision and Pattern Recognition*, pages 19711–19722, 2024. 3
- [33] Haotong Lin, Sida Peng, Zhen Xu, Tao Xie, Xingyi He, Hujun Bao, and Xiaowei Zhou. High-fidelity and real-time novel view synthesis for dynamic scenes. In *SIGGRAPH Asia Conference Proceedings*, 2023. 1, 3
- [34] Xinqi Liu, Chenming Wu, Xing Liu, Jialun Liu, Jinbo Wu, Chen Zhao, Haocheng Feng, Errui Ding, and Jingdong Wang. Gea: Reconstructing expressive 3d gaussian avatar from monocular video. *arXiv preprint arXiv:2402.16607*, 2024. 3
- [35] Yang Liu, Xiang Huang, Minghan Qin, Qinwei Lin, and Haoqian Wang. Animatable 3d gaussian: Fast and high-quality reconstruction of multiple human avatars. *arXiv preprint arXiv:2311.16482*, 2023. 3
- [36] Yu-Lun Liu, Chen Gao, Andreas Meuleman, Hung-Yu Tseng, Ayush Saraf, Changil Kim, Yung-Yu Chuang, Johannes Kopf, and Jia-Bin Huang. Robust Dynamic Radiance Fields. In *Proceedings of the IEEE/CVF Conference on Computer Vision and Pattern Recognition*, pages 13–23, 2023. 3
- [37] Matthew Loper, Naureen Mahmood, Javier Romero, Gerard Pons-Moll, and Michael J Black. Smpl: A skinned multi-person linear model. *ACM Transactions on Graphics*, 34(6), 2015. 1, 2, 3
- [38] Ben Mildenhall, Pratul P Srinivasan, Matthew Tancik, Jonathan T Barron, Ravi Ramamoorthi, and Ren Ng. Nerf: Representing scenes as neural radiance fields for view synthesis. In *European Conference on Computer Vision*, pages 405–421, 2020. 1, 2
- [39] Arthur Moreau, Jifei Song, Helisa Dharmo, Richard Shaw, Yiren Zhou, and Eduardo Pérez-Pellitero. Human gaussian splatting: Real-time rendering of animatable avatars. In *Proceedings of the IEEE/CVF Conference on Computer Vision and Pattern Recognition*, pages 788–798, 2024. 3
- [40] Haokai Pang, Heming Zhu, Adam Kortylewski, Christian Theobalt, and Marc Habermann. Ash: Animatable gaussian splats for efficient and photoreal human rendering. In *Proceedings of the IEEE/CVF Conference on Computer Vision and Pattern Recognition*, pages 1165–1175, 2024. 3
- [41] Sunghoon Park, Minjung Son, Seokhwan Jang, Young Chun Ahn, Ji-Yeon Kim, and Nahyup Kang. Temporal Interpolation Is All You Need for Dynamic Neural Radiance Fields. In *Proceedings of the IEEE/CVF Conference on Computer Vision and Pattern Recognition*, pages 4212–4221, 2023. 3
- [42] Georgios Pavlakos, Vasileios Choutas, Nima Ghorbani, Timo Bolkart, Ahmed A. A. Osman, Dimitrios Tzionas, and Michael J. Black. Expressive body capture: 3D hands, face, and body from a single image. In *Proceedings IEEE Conf. on Computer Vision and Pattern Recognition (CVPR)*, pages 10975–10985, 2019. 1, 2, 3
- [43] Sida Peng, Yuanqing Zhang, Yinghao Xu, Qianqian Wang, Qing Shuai, Hujun Bao, and Xiaowei Zhou. Neural body: Implicit neural representations with structured latent codes for novel view synthesis of dynamic humans. In *CVPR*, 2021. 3, 5
- [44] Zhiyin Qian, Shaofei Wang, Marko Mihajlovic, Andreas Geiger, and Siyu Tang. 3dgs-avatar: Animatable avatars via deformable 3d gaussian splatting. In *Proceedings of the IEEE/CVF Conference on Computer Vision and Pattern Recognition*, pages 5020–5030, 2024. 1, 3, 4, 6, 7, 2
- [45] Ruizhi Shao, Zerong Zheng, Hanzhang Tu, Boning Liu, Hongwen Zhang, and Yebin Liu. Tensor4d: Efficient Neural 4D Decomposition for High-fidelity Dynamic Reconstruction and Rendering. In *Proceedings of the IEEE/CVF Conference on Computer Vision and Pattern Recognition*, pages 16632–16642, 2023. 3
- [46] Qing Shuai, Chen Geng, Qi Fang, Sida Peng, Wenhao Shen, Xiaowei Zhou, and Hujun Bao. Novel view synthesis of human interactions from sparse multi-view videos. In *SIGGRAPH Conference Proceedings*, 2022. 2
- [47] Shaofei Wang, Katja Schwarz, Andreas Geiger, and Siyu Tang. Arah: Animatable volume rendering of articulated human sdf. In *European conference on computer vision*, pages 1–19. Springer, 2022. 3
- [48] Zhou Wang, Alan C Bovik, Hamid R Sheikh, and Eero P Simoncelli. Image Quality Assessment: from Error Visibility to Structural Similarity. *IEEE transactions on image processing*, 13(4):600–612, 2004. 3, 7
- [49] Chung-Yi Weng, Brian Curless, Pratul P Srinivasan, Jonathan T Barron, and Ira Kemelmacher-Shlizerman. Hu-

- mannerf: Free-viewpoint rendering of moving people from monocular video. In *Proceedings of the IEEE/CVF conference on computer vision and pattern Recognition*, pages 16210–16220, 2022. 3, 5
- [50] Wenqi Xian, Jia-Bin Huang, Johannes Kopf, and Changil Kim. Space-time Neural Irradiance Fields for Free-viewpoint Video. In *Proceedings of the IEEE/CVF Conference on Computer Vision and Pattern Recognition*, pages 9421–9431, 2021. 3
- [51] Zhen Xu, Sida Peng, Haotong Lin, Guangzhao He, Jiaming Sun, Yujun Shen, Hujun Bao, and Xiaowei Zhou. 4k4d: Real-time 4d view synthesis at 4k resolution. In *CVPR*, 2024. 1, 3
- [52] Richard Zhang, Phillip Isola, Alexei A Efros, Eli Shechtman, and Oliver Wang. The Unreasonable Effectiveness of Deep Features as a Perceptual Metric. In *Proceedings of the IEEE conference on computer vision and pattern recognition*, pages 586–595, 2018. 7
- [53] Shunyuan Zheng, Boyao Zhou, Ruizhi Shao, Boning Liu, Shengping Zhang, Liqiang Nie, and Yebin Liu. Gps-gaussian: Generalizable pixel-wise 3d gaussian splatting for real-time human novel view synthesis. In *Proceedings of the IEEE/CVF Conference on Computer Vision and Pattern Recognition*, pages 19680–19690, 2024. 3
- [54] Yang Zheng, Qingqing Zhao, Guandao Yang, Wang Yifan, Donglai Xiang, Florian Dubost, Dmitry Lagun, Thabo Beeler, Federico Tombari, Leonidas Guibas, et al. Physavatar: Learning the physics of dressed 3d avatars from visual observations. *arXiv preprint arXiv:2404.04421*, 2024.
- [55] Wojciech Zielonka, Timur Bagautdinov, Shunsuke Saito, Michael Zollhöfer, Justus Thies, and Javier Romero. Drivable 3d gaussian avatars. *arXiv preprint arXiv:2311.08581*, 2023. 3

# GAST: Sequential Gaussian Avatars with Hierarchical Spatio-temporal Context

## Supplementary Material

### 7. Details of Skeleton Motion $\Delta P$

The pose  $P$  is represented as the rotations of all joints in axis-angle form:

$$P = \{\theta_1, \theta_2, \dots, \theta_K\}, \quad (24)$$

where  $\theta_j \in \mathbb{R}^3$  describes the  $j$ -th joint’s relative rotation with its parent in axis-angle form [37]. We follow Dyco [5] to derive each joint’s rotation variation  $\Delta\theta$  between adjacent frames as its skeleton motion representation. Specifically, the rotation of  $j$ -th joint in matrix form can be obtained according to *Rodrigues formula* [37]:

$$\mathbf{R}_j = \text{Rodrigues}(\theta_j), \quad (25)$$

where  $\mathbf{R}_j$  is a  $3 \times 3$  rotation matrix. Given 2 consecutive poses  $P^t$  and  $P^{t-s}$ , the temporal variation of  $j$ -th joint’s rotation is computed as a relative transformation matrix  $\Delta\mathbf{R}_j^t$ :

$$\Delta\mathbf{R}_j^t = \mathbf{R}_j^t \mathbf{R}_j^{t-s-1}. \quad (26)$$

Then we convert the  $3 \times 3$  matrix  $\Delta\mathbf{R}_j^t$  back to the axis-angle form  $\Delta\theta_j^t \in \mathbb{R}^3$ . Now, the skeleton motion at time  $t$  is

$$\Delta P^t = \{\Delta\theta_1^t, \Delta\theta_2^t, \dots, \Delta\theta_K^t\}, \quad (27)$$

which is simplified as  $\Delta P^t = \delta(P^t, P^{t-s})$  in Eq. (7).

### 8. Datasets

**I3D-Human Dataset [5]** We use images with resolution  $512 \times 512$  for experiments following Dyco [5].

**DNA-Rendering Dataset [6]** We use the original images’ resolution  $512 \times 612$  for experiments. For the dataset split, we sample 24 evenly distributed views from camera IDs 0–48 for training and 6 additional uniformly distributed views from IDs 48–60 for novel view testing.

### 9. Motion Embeddings for Non-Rigid MLP

The embeddings  $f_{\Delta P}$  and  $f_{\mathcal{V}}$  in Eq. (12) describe the skeleton and local region motions, respectively. For each frame, all Gaussian primitives  $\{\mathcal{G}_i\}$  share the same skeleton motion embedding  $f_{\Delta P} \in \mathbb{R}^{32}$  and we concat it with  $\mathcal{G}_i$ ’s point-wise motion embedding  $f_{\mathcal{V}_i} \in \mathbb{R}^{64}$  as a new condition  $f'_i \in \mathbb{R}^{96}$ .  $f'_i$  is then input to a 2-layer MLP  $\mathcal{E}_{non-rigid}$  to predict the corresponding non-rigid deformation.

### 10. Details of Loss Functions

$\mathcal{L}_{color}$  is the  $L_1$  loss between the rendered image  $I$  and the ground truth  $I_{gt}$ :

$$\mathcal{L}_{color} = |I - I_{gt}|. \quad (28)$$

We use  $\mathcal{L}_{ssim}$  to constrain the structure similarity between rendered image and the ground truth, which is given by

$$\mathcal{L}_{ssim} = 1 - \text{SSIM}(I, I_{gt}), \quad (29)$$

where  $\text{SSIM}(\cdot)$  is the SSIM metric. Additionally, we use the LPIPS loss to ensure the perceptual similarity:

$$\mathcal{L}_{lpiPs} = \text{LPIPS}(I, I_{gt}), \quad (30)$$

where  $\text{LPIPS}(\cdot)$  is the LPIPS metric. Following GauHuman [17] and 3DGS-Avatar [44], we employ a mask loss to ensure that Gaussian primitives are accurately localized within their designated regions:

$$\mathcal{L}_{mask} = \|M - M_{gt}\|_2 \quad (31)$$

where  $M_{gt}$  is the foreground mask and  $M$  is the accumulated  $\alpha$  value:

$$M = \sum \alpha_i \prod_{j=1}^{i-1} (1 - \alpha_j). \quad (32)$$

### 11. Details of Optimization

In our experiments, the number  $|\mathcal{S}|$  (in Eq. (16)) of sequence sampled in different scales is set to 3 and each sequence length  $L$  (in Eq. (6)) is set to 8. We use the  $\tau = 8$  nearest SMPL template vertexes’ velocities to get each Gaussian primitive’s local velocity embedding  $e_i$  (in Eq. (11)). Additionally, we utilize the adaptive densification in [23] to control the number of Gaussian primitives.

For DNA-Rendering dataset, we use the SMPL-X [42] model with pose dimension  $P \in \mathbb{R}^{25 \times 3}$  in our experiments. We adopt the SMPL-X template with  $N = 10475$  vertexes as Gaussian initialization. We optimize 30k iterations and set the loss weights  $\lambda_0 = 1.0, \lambda_1 = 0.01, \lambda_2 = 0.01$ . The initial sampling step and the increasing interval are  $s_0 = 1$  and  $\Delta s = 2$ , respectively. The final sample scales are  $\mathcal{S} = \{1, 3, 5\}$  (in Eq. (16)). For I3D-Human dataset, we follow Dyco [5] to use SMPL [37] model in our experiments for fairness. The number of SMPL template vertexes used for Gaussian initialization is  $N = 6890$  and the corresponding pose dimension is  $P \in \mathbb{R}^{23 \times 3}$ . We optimize 15k iterations



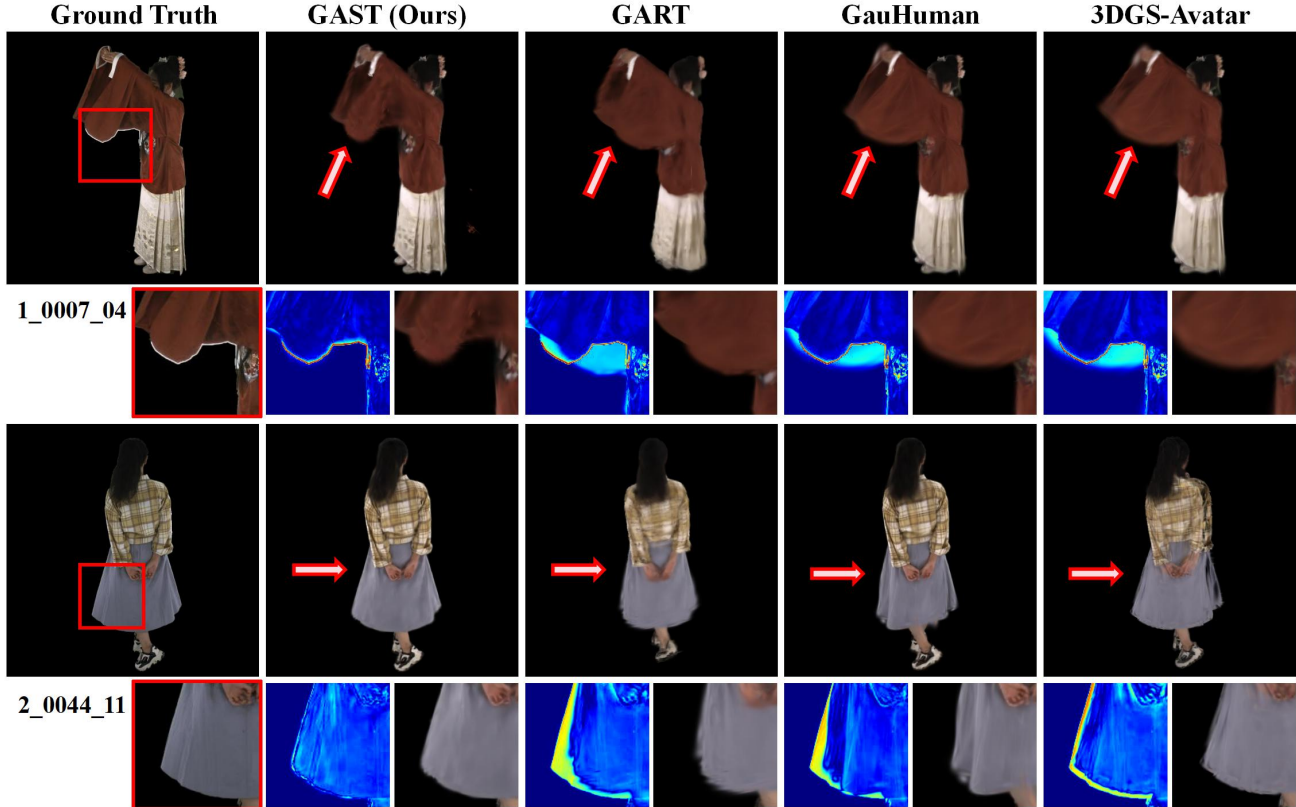


Figure 6. **Additional Novel View Qualitative Results on DNA-Rendering Dataset [6].** We provide both the complete image and localized error map comparisons against other methods for a more comprehensive visualization.

and set the loss weights  $\lambda_0 = 1.0, \lambda_1 = 0.1, \lambda_2 = 0.1$ . We set the increasing interval  $\Delta s = 9$ . The initial sampling step is  $s_0 = 24$  and the final sample scales are  $\mathcal{S} = \{24, 33, 42\}$  (in Eq. (16)). Note that the experiment in Tab. 3 (d) adopts single sampling step that  $\mathcal{S} = \{s_0\}$ .

## 12. Additional Results

### 12.1. Comparisons of Novel View Rendering

Fig. 6 shows additional qualitative comparisons with other SOTA methods on the DNA-Rendering dataset [6]. Our approach excels in regions where motion causes notable appearance variations, producing results that conform to the true shape more accurately, as exemplified by the sleeve (top row) and the skirt hem (bottom row) in Fig. 6.

### 12.2. Comparisons of Novel Pose Rendering

Tab. 4 reports the quantitative results of novel pose rendering on the I3D-Human dataset [5]. Our method achieves competitive performance compared with SOTA human modeling methods. Fig. 7 shows the qualitative comparisons of novel pose rendering and we utilize error maps to visualize the differences between various methods

Table 4. **Quantitative Results of Novel Pose Renderings on I3D-Human Dataset.**

Methods	PSNR $\uparrow$	SSIM $\uparrow$	LPIPS* $\downarrow$
3DGS-Avatar [44]	29.53	0.9554	38.58
Dyco [5]	30.30	0.9582	33.52
GauHuman [17]	29.31	0.9525	48.29
GAST(Ours)	30.39	0.9582	38.15

more clearly. Compared to Dyco [5], which relies solely on joint motions as conditions, our GAST leverages the motion state of each Gaussian primitive to predict deformations, enabling more flexible modeling of motions in regions distant from the human body. The shape of the clothing in Fig. 7 demonstrates that our method can render the appearance consistent with the novel pose motion, leading to more accurate results.

## 13. Additional Ablations

**Different Sample Steps** Tab. 5 shows the quantitative metrics with different sequential sampling steps. The results demonstrate that combining all coarse-to-fine temporal motions as the condition leads to more robust non-rigid

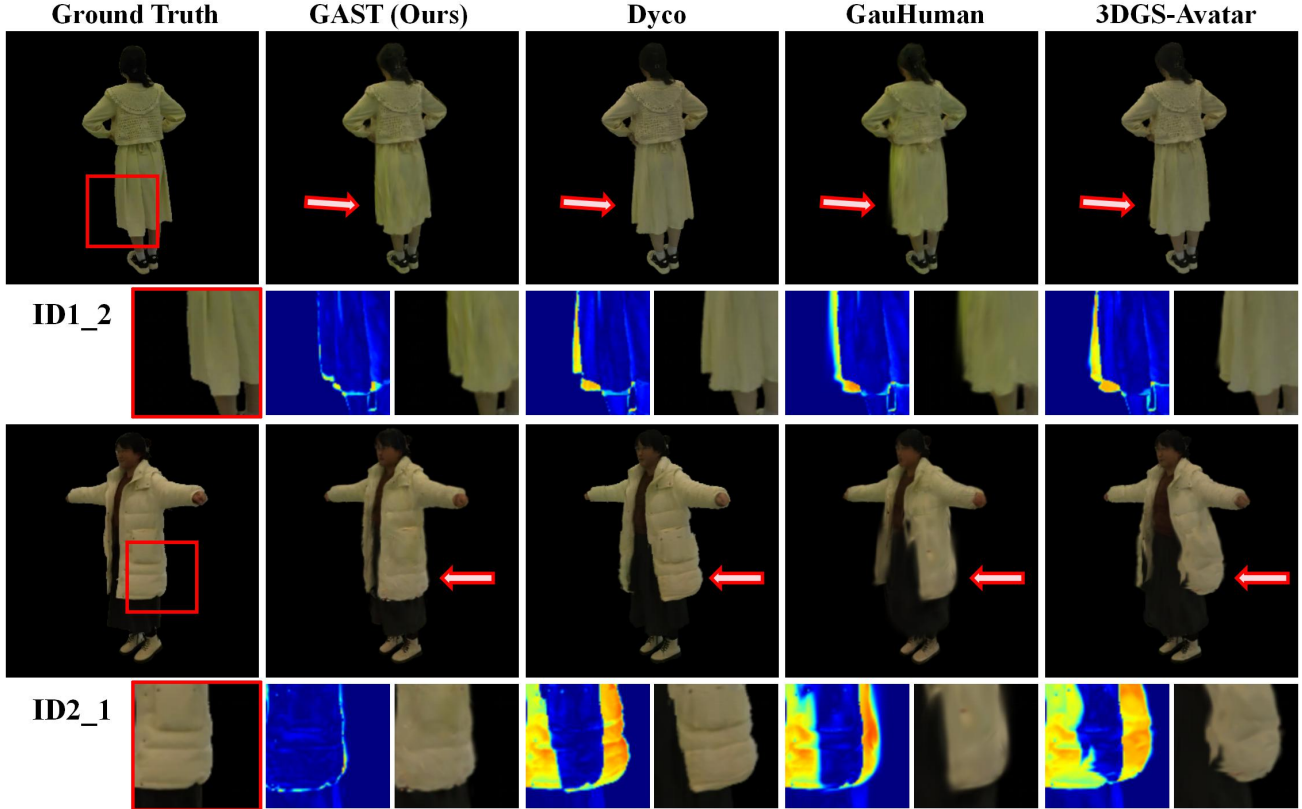


Figure 7. Additional Novel Pose Qualitative Results on I3D-Human Dataset [5].

deformation and better performance.

Table 5. Impact of Different Sampling Steps on I3D-Human.

Sampling Step $\mathcal{S}$	PSNR $\uparrow$	SSIM $\uparrow$	LPIPS* $\downarrow$
$\mathcal{S} = \{24\}$	32.05	0.96468	32.82
$\mathcal{S} = \{33\}$	32.04	0.96467	33.06
$\mathcal{S} = \{42\}$	32.06	0.96472	32.87
$\mathcal{S} = \{24, 33, 42\}$	<b>32.13</b>	<b>0.96476</b>	<b>32.65</b>

**Different KNN Sampled Vertices** Tab. 6 presents the quantitative results on I3D-Human dataset [5] with different numbers of KNN vertices when deriving the velocity  $e_i$  of each Gaussian primitive (Eq. 11). It suggests that considering the motion states of all local regions helps obtain a more robust Gaussian primitive’s velocity embedding, contributing to enhancing performance.

Table 6. Impact of Different KNN Vertex Number  $\tau$ .

KNN num. $\tau$	$\tau = 1$	$\tau = 3$	$\tau = 6$	$\tau = 8$
PSNR $\uparrow$	32.06	32.07	32.08	<b>32.13</b>